

Impact of string connection and contact defects on electrical current distribution in solar cells and modules: A model validated by magnetic field imaging

Ammar Tummalieh^{1,2}  | Max Mittag¹ | Julian Weber¹  | Damla Yucebas¹ | Levin Schäfer¹ | Rüdiger Quay^{2,3} | Christian Reichel¹ | Holger Neuhaus¹

¹Fraunhofer Institute for Solar Energy Systems ISE, Freiburg, Germany

²Department of Microsystems Engineering (IMTEK), University of Freiburg, Freiburg, Germany

³Fraunhofer Institute for Applied Solid State Physics IAF, Freiburg, Germany

Correspondence

Ammar Tummalieh, Fraunhofer Institute for Solar Energy Systems ISE, Heidenhofstrasse 2, Freiburg 79110, Germany.

Email: ammar.tummalieh@ise.fraunhofer.de

Funding information

German Ministry of Economic Affairs and Energy, Grant/Award Number: 03EE1028A "CTS1000plus"

Abstract

Modeling of solar modules and their components is essential to quantify geometrical, optical, and electrical losses and to improve the designs and technologies in terms of performance. In most loss analysis models, the current share among the busbars of the solar cell is assumed to be equal since a symmetrical distribution of the metallization is given. The impact of string terminal connection on the current distribution among the ribbons and the resulting changes in ohmic losses has not been studied yet. In this study, a MATLAB model is developed to consider the impact of the string connector terminal position on the current distribution and the ohmic losses in the ribbons and in string connector. The model allows for the analysis of the impact of contact defects scenarios in ribbons and string connectors on the current distribution. Results show that the highest current flows at the closest busbar to the string connector terminal while the current decreases at the busbars farther away from the terminal due to higher ohmic resistance of the current path. The higher the ohmic resistance of the string connector, the more inhomogeneous the current share at busbars. Simulating a 9 busbar M6 half-cell with $1 \times 0.08 \text{ mm}^2$ string connector, positioning the string connector terminal at the leftmost or rightmost ribbon results in 0.4 W less power compared to center connection configuration, where the string connector terminal is positioned at the center ribbon. Furthermore, simulation results show that inhomogeneity of current causes about 2.1% reduction in module power compared to the case of evenly distributed cell current, considering a 120-half-cell module with the same string connector. Regarding contact defect analysis, exemplary simulations show the impact of the position of detached ribbons on the power or efficiency loss. Considering left or right connection configuration, detaching the leftmost or rightmost ribbon results in higher power loss compared to other ribbons. Detaching one cell ribbon completely from the string connector results in about 0.2%_{abs} decrease in cell efficiency, while detaching the outer ribbon along all strings of a 120-half-cell module results in power loss of about 0.8%. The developed

model is validated by performing magnetic field imaging (MFI) measurements, in which the magnetic flux density induced by the current carried by the ribbons is measured.

KEY WORDS

characterization, contact defects, current inhomogeneity, magnetic field imaging, modeling, PV module, simulation, solar cell, string connection

1 | INTRODUCTION

Photovoltaic (PV) technology is recently evolving rapidly, and solar cells with higher performance and efficiencies are being developed, manufactured, and integrated into PV modules. On the one hand, improving the design, materials, and manufacturing technologies is necessary to achieve high performance solar cells and modules. On the other hand, the reliability of characterization techniques being used is equally important to accurately evaluate the improvements.¹ As part of some published studies of PV cell and module modeling,^{2–5} analytical models have been developed to define geometrical, optical, and electrical losses that take place on cell and module level. In the developed models, solar cell current share among the busbars is assumed to be equal for all busbars when a symmetrical distribution of the metallization is assumed. The impact of the external connection of the solar cell on the current distribution over the busbars and the resulting ohmic losses has not been studied yet, except on different analytical measurements such as electroluminescence.⁶ The impact of the current distribution on the *I*-*V* characteristic of the solar cell was studied in Zekry and Al-Mazroo and Rajput et al.^{7,8} and referred to the partial metallization of the front side of the solar cell. An important aspect that has not been investigated yet is the impact of the string connection on the current distribution among the ribbons and cell power and efficiency. Additionally, modeling of solar cells and PV modules considering defects scenarios such as detached ribbons is essential when analyzing the performance of modules under realistic conditions. In that regard, cell interconnection and series resistance are investigated in several studies^{9–11} by applying mechanical stress analysis electroluminescence imaging but without linking that to electrical output of the solar cell or PV module. In the present study, the influence of the position and the dimensions of the string connection on the current distribution among the busbars of the solar cell and therefore on the ohmic losses that take place is investigated. In addition, the contact between the solar cell's metallization and the ribbon including solder or electrically conductive adhesive (ECA) layer is modeled, considering different contact resistance components. This helps to simulate different contact defects scenarios and its impact on the solar cell output. The findings are validated by characterizing solar cells with different string connection configurations by applying magnetic field imaging (MFI) measurements.^{12–14}

2 | METHOD

Using a bottom-up multiphysics model,^{2–5} different gain and loss channels from solar cell to module level can be calculated. The starting point of this cell-to-module (CTM) analysis are the solar cell parameters at standard test conditions (STC). The solar cell *I*-*V* curve is calculated based on the single diode model.¹⁵ Based on the *I*-*V* curve, the maximum power point parameters of the solar cell can be extracted. To analyze the different gain and loss channels, the solar cell *I*-*V* curve is adapted based on different optical loss and gain factors such as glass reflection and absorption as well as light coupling within the module. Furthermore, the electrical losses that take place in the ribbons as well as in the string connectors are considered. This work focuses on the electrical losses of the analysis and the effect of the inhomogeneity of the solar cell current on its power and efficiency. In the methodology section, the analytical model that is used to calculate the electrical current distribution and electrical losses as well as the contact resistance is presented. The validation using MFI measurements is also explained.

2.1 | Geometrical parameterization

The first step is to geometrically parameterize the solar cell as exemplary shown in Figure 1 for the front side. The backside is parameterized in the same way.

Since the solar cell current can be assumed to be directly proportional to the irradiance and therefore to the solar cell active area,¹⁶ the area is used to scale the electrical current for different metallization sections.

In Table 1, all geometrical parameters shown in Figure 1 are declared.

Calculating the ohmic losses in the interconnected solar cells requires determining the electrical current that is collected from the solar cell active area in each metallization part, that is, continuous busbar or contact pad. To that end, the pad specific electrical current is calculated by defining the solar cell active area around each metallization part, that is, $A_{O|i,j}$, using the solar cell maximum power point current I_{mpp} and geometrical information shown in Figure 1 and described in Table 1. The indices *i* and *j* are used to distinguish the

FIGURE 1 Geometrical parameterization of the front side of an exemplary solar cell. White parts represent contact pads of the cell. Dashed black lines build the area of interest (AOI) of each contact pad.

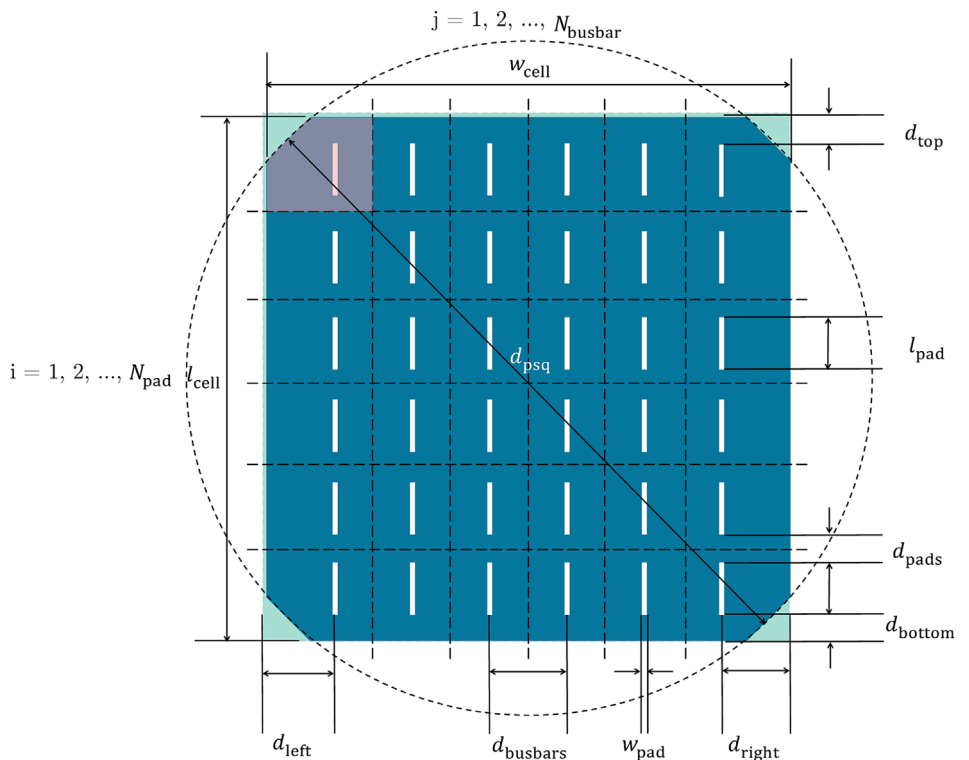


TABLE 1 Parameters of the solar cell geometry.

Symbol	Quantity
l_{cell}	Length of the solar cell
w_{cell}	Width of the solar cell
N_{busbar}	Number of busbars
N_{pad}	Number of contact pads per busbar
d_{psq}	Pseudo-square diameter of the ingot
l_{pad}	Length of contact pad
w_{pad}	Width of contact pad
d_{pads}	Vertical distance between contact pads
d_{busbars}	Horizontal distance between busbars
d_{left}	Left distance between contact pad/busbar and cell edge
d_{right}	Right distance between contact pad/busbar and cell edge
d_{top}	Top distance between contact pad/busbar and cell edge
d_{bottom}	Bottom distance between contact pad/busbar and cell edge

$$I_{ij} = I_{\text{mpp}} \frac{AOI_{ij}}{A_{\text{cell}}} \quad (2)$$

2.2 | Power loss

Connecting conventional solar cells in series normally requires soldering of ribbons to the solar cell metallization. The flowing current from a cell to another through the ribbons results in dissipated power that is linearly dependent on the square of the flowing current's magnitude and to the ohmic resistance of the ribbon. Considering the trend of the current and assuming no direct contact between cell active area and ribbon, the ribbon can be mainly categorized into soldered and unsoldered ribbon sections as shown in Figure 2.¹⁷

Regarding the soldered ribbon sections, the ribbon is directly connected to the cell metallization, that is, busbars or contact pads, which collect the electrical current from the fingers and cell's active area. The electrical current I in these ribbon sections rises linearly over the distance x and can be described within a single contact pad using the function $I(x)$ as follows.

$$I(x) = \frac{I_{\text{pad}}}{L_{\text{pad}}} x \quad (3)$$

pads within each busbar and the busbars within the cell, respectively. Exemplary red highlighted area of interest ($AOI_{1,1}$) illustrated in Figure 1 can be calculated as follows.

$$AOI_{1,1} = \left(d_{\text{left}} \frac{d_{\text{busbars}}}{2} \left(d_{\text{top}} + l_{\text{pad}} + \frac{d_{\text{pads}}}{2} \right) \right) - A_{\text{corner}} \quad (1)$$

Based on the calculated AOI , the pad specific current I_{ij} of the i^{th} contact pad in the j^{th} busbar of the solar cell can be calculated as follows.

The power loss in a ribbon section that is soldered or glued to a contact pad $P_{\text{rib,sol}}$ with ribbon resistivity ρ_{ribbon} and cross section area A_{ribbon} can be calculated by applying the integration as shown in the following equation, where R_{ribbon} is the resistance of the ribbon section.

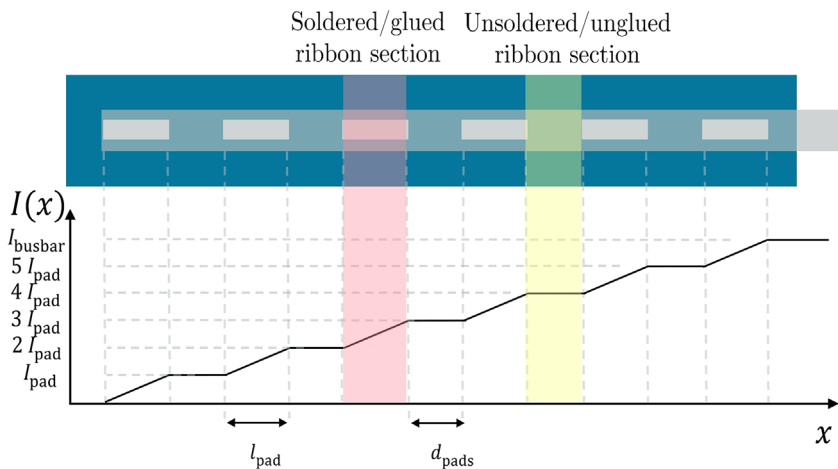


FIGURE 2 Electrical current along a ribbon soldered/glued to a non-continuous busbar containing 6 contact pads as a function of the distance. Exemplary soldered/glued and unsoldered ribbon sections are highlighted with red and yellow, respectively.

$$P_{\text{rib,sol}} = \frac{\rho_{\text{ribbon}}}{A_{\text{ribbon}}} \frac{I_{\text{pad}}^2}{l_{\text{pad}}^2} \int_0^{l_{\text{pad}}} x^2 \cdot dx = \frac{1}{3} R_{\text{ribbon}} I_{\text{pad}}^2 \quad (4)$$

The unsoldered ribbon sections are only overlapping the cell active area or located in the gaps between two cell edges and are not directly connected to the cell metallization. The flowing current in these ribbon sections is constant. Within this analysis, it is assumed that current is only collected at the metallized area. The power loss in an unsoldered ribbon section $P_{\text{rib,unsol}}$ can be calculated using the following equation.

$$P_{\text{rib,unsol}} = R_{\text{ribbon}} I_{\text{pad}}^2 \quad (5)$$

For a solar cell with number of busbars N_{busbars} and number of contact pads per busbar N_{pads} that is connected in series within a string with cell distance d_{cell} as shown in Figure 3, the power loss can be categorized depending on the resistance of the ribbon and the current flowing through it.

The power loss in the ribbons on a solar cell's front side can be calculated using the following equation.

$$P_{\text{loss,cell}_{\text{front}}} = \sum_{j=1}^{N_{\text{busbars}}} \sum_{i=1}^{N_{\text{pads}}} P_{\text{loss},l_{\text{pad}}} + \sum_{j=1}^{N_{\text{busbars}}} \sum_{i=1}^{N_{\text{pads}}-1} P_{\text{loss},d_{\text{pads}}} + \sum_{j=1}^{N_{\text{busbars}}} (P_{\text{loss},d_{\text{top}}} + P_{\text{loss},d_{\text{cell}}}) \quad (6)$$

For the total power loss of the backside $P_{\text{loss,cell}_{\text{back}}}$, the backside metallization pattern is considered using the same approach and considering power loss in the ribbon section at the top $P_{\text{loss},d_{\text{top}}}$ instead of power loss in the ribbon section at the bottom $P_{\text{loss},d_{\text{bottom}}}$. In case of a solar cell with continuous busbar, same approach is applied using $N_{\text{pads}} = 1$, and $d_{\text{pads}} = 0$.

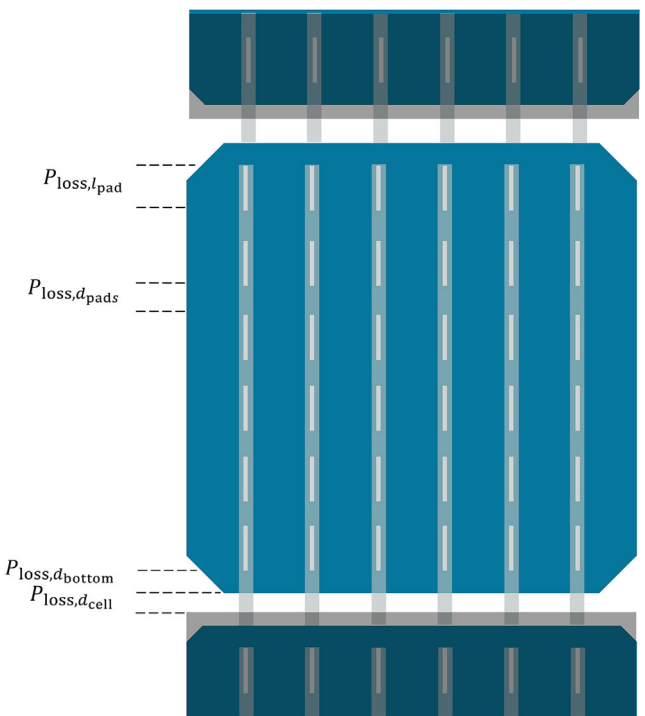


FIGURE 3 Solar cell connected in series within a string with different power loss sections illustrated.

2.3 | String connection

To build a full-scale PV module, solar cells are typically interconnected in series to strings. Strings can be connected in series or in parallel to reach certain module voltage and current. At the terminals of a string, the ribbons of the top and bottom cells are soldered to string connectors to collect the busbars' current and conduct it to the next string

FIGURE 4 Different string connection configurations. (A) Front-right back-right, (B) front-left back-right, (C) front-middle back-middle, (D) front-left back-left, and (E) front-right back-left.

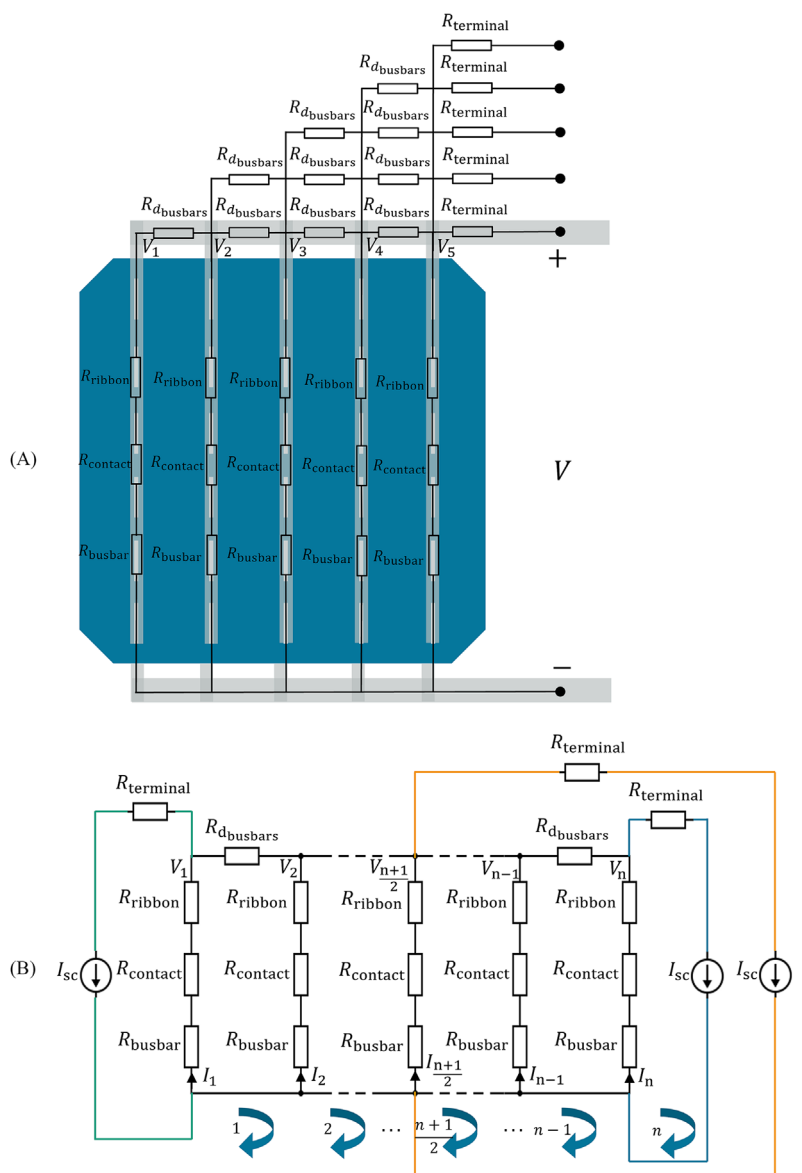
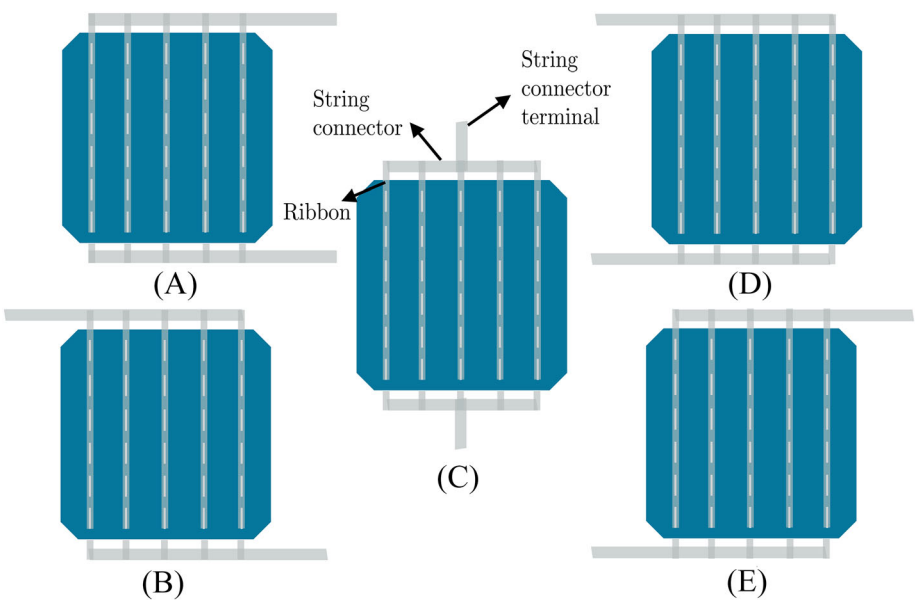


FIGURE 5 (A) Resistance of current path of an exemplary 5-busbar solar cell connected using right string connector configuration and (B) the electrical circuit used to calculate the current at busbar applying left (green), middle (orange), and right (blue) string connector configurations. Loops used in the mesh analysis are numbered.

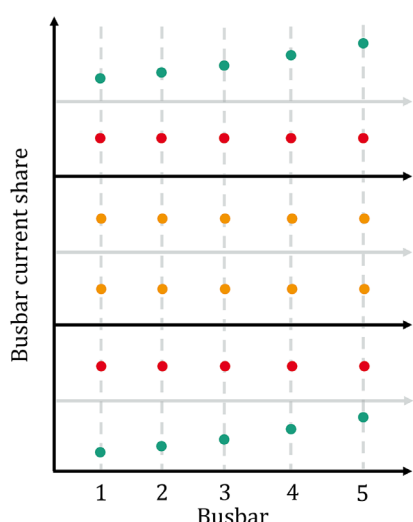
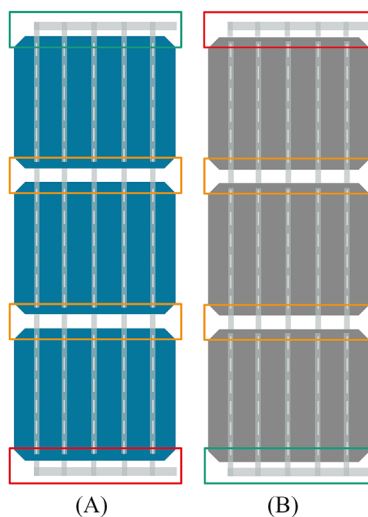


FIGURE 6 (A) The front and (B) back sides of a string containing 3 cells in series. The green border indicates direct connection between string connector and ribbons. Orange border indicates a ribbon-to-ribbon connection. Red border indicates no direct connection between string connector and ribbons. The current share at busbars is shown on the right side with color-coded points.

and finally to the junction box. Whereas single cell modules for laboratory investigations often have a string terminal at the middle of the string connector, strings within a PV module may have different string connection configurations depending on their position and the connection type. In Figure 4, different string connection configurations are illustrated.

By considering the string connection, the ohmic resistance of the current path between each ribbon-string connector joint and the end of the string connector terminal affects the magnitude of the current flowing in each ribbon. Due to different distances between each ribbon-string connector joint and the end of the string connector terminal, different voltage drops occur across the ohmic resistance of the string connector. The longer the distance between the ribbon-string connector joint and the end of the string connector terminal, the higher the effective ohmic resistance of configuration and the higher the voltage drop between the connector and the most distant ribbon. If the string connector resistance is not neglected, the current share among the busbars will not be identical.

As illustrated in Figure 5, ribbon-contacted solar cells can be characterized by performing *I-V* measurement, where an external voltage *V* is applied to the solar cell.¹⁸ Due to the different additional ohmic resistances of the string connector with respect to each busbar as shown in the exemplary solar cell in Figure 5A, voltage drops take place over the string connector resistances $R_{d_{busbars}}$. Figure 5B shows the electrical circuit used to calculate the ribbon currents by applying different string connector configurations. The voltage at any ribbon-string connector joint V_n can be calculated using mesh analysis by applying Kirchhoff's voltage law to the n loops. The current at the busbar can be calculated using the joint voltage and the busbar, ribbon, and contact resistances. For the sake of simplicity of the MATLAB analytical model, the resistance of the fingers is neglected since it is much higher than the resistance of the connectors. In other words, it is assumed that there is no lateral current flow inside the solar cell between busbars. The mesh analysis equation

for loop 1 considering right connection configuration (blue) can be expressed as follows.

$$I_1(R_{busbar} + R_{contact} + R_{ribbon}) + I_2(R_{d_{busbars}}) + (I_1 - I_2)(R_{ribbon} + R_{contact} + R_{busbar}) = 0 \quad (7)$$

In single cell modules such as the one in Figure 5, both the front and the back sides are simultaneously affected by the string connection configuration. Considering multi-cell strings, only the side of the cell that is directly connected to the string connector is affected. In Figure 6, the front and back sides of a 3-cell-string with corresponding exemplary trend of current share at busbars are illustrated.

2.4 | Contact resistance

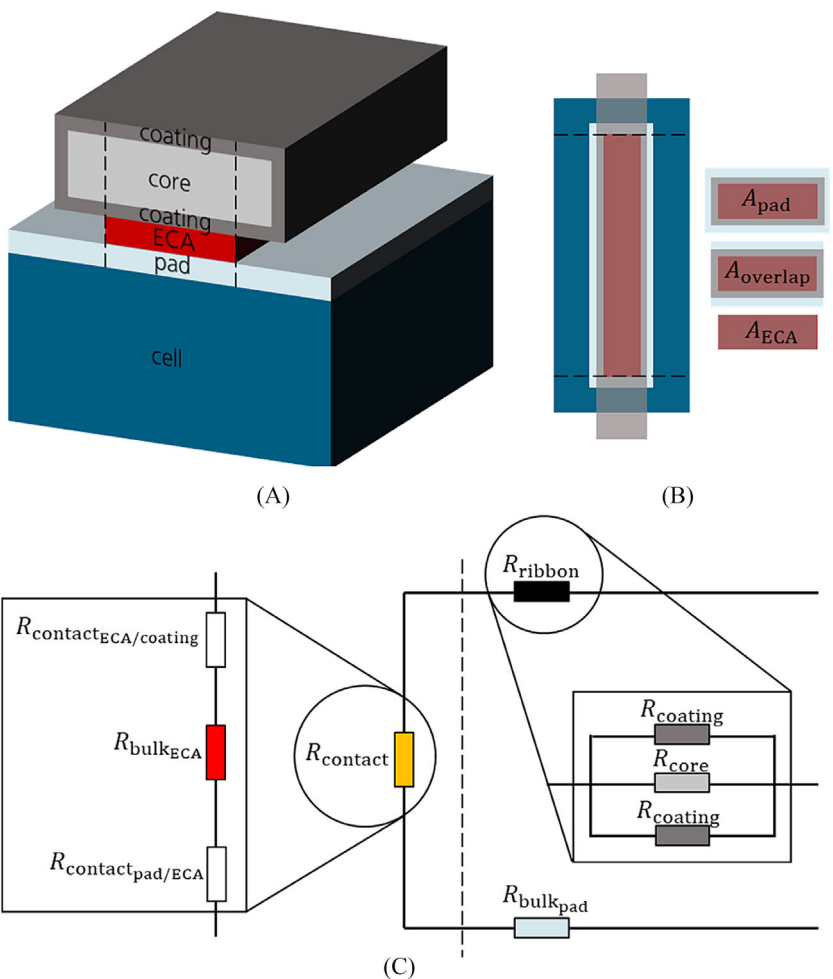
To depict contact defects between the solar cell metallization and the interconnection ribbons, a model that describes the different contact resistance components is developed. The method employed to calculate the contact resistance is implemented on glued ribbons using ECA. The same methodology is also applicable when considering soldered ribbons. The different resistance components of the contact between ribbon and contact pad are illustrated in Figure 7.

To calculate the equivalent resistance, the ohmic resistance of the ECA bulk is calculated based on its electrical resistivity ρ_{ECA} , thickness t_{ECA} , and area A_{ECA} as shown in the following equation.

$$R_{ECA\text{ (bulk)}} = \frac{\rho_{ECA} t_{ECA}}{A_{ECA}} \quad (8)$$

However, the ECA area A_{ECA} is not necessarily equal to the pad or ribbon area. In that case, it is calculated using the following equation, where f_{share} represents the area share of the ECA with respect to the overlap area $A_{overlap}$.

FIGURE 7 (A) Cross section, (B) top view, and (C) equivalent circuit of the contact resistance layer structure between cell metallization and a glued ribbon using ECA.



$$A_{\text{ECA}} = \frac{f_{\text{share}} A_{\text{overlap}}}{100\%} \quad (9)$$

The contact resistance between the metallization and ECA as well as between ECA and coating can be calculated using the contact area resistivity of pad/ECA or ECA/coating ρ_{contact} and the area of the ECA A_{ECA} as shown in the following equation.

$$R_{\text{contact}} = \frac{\rho_{\text{contact}}}{A_{\text{ECA}}} \quad (10)$$

The contact resistance between ribbon and a single contact pad can be calculated by summarizing the three calculated resistance components.

The contact defect is modeled by increasing the contact resistance between ribbon and contact pad. This can be realized by either increasing the contact resistivity ρ_{contact} or decreasing the area of the ECA A_{ECA} . In this part of the model, lateral currents must be considered, and therefore, the finger are included. In Figure 8, the redistribution of current in case of contact failure at a certain pad is illustrated in (a) with the corresponding used current divider circuit in (b), assuming horizontally transportation of current through fingers.

In case of a complete contact failure at a contact pad, the current collected from the AOI of the concerned pad is assumed to be distributed to the neighboring busbars according to the distance between them. For that, a current divider circuit is used to consider different current paths (finger lengths) to calculate the current distribution depending on their resistances. In all affected ribbons, the current accumulation that is explained in Figure 2 would change and therefore the ohmic losses in the ribbons as well as in the string connector. To exemplary calculate the current I_x flowing from the degraded pad to the furthest busbar (green) through fingers as shown in Figure 8B, the following equation can be used, where R_{eq} is the equivalent resistance of the parallel connection.

$$I_x = \frac{R_{\text{eq}}}{3 R_{\text{finger}}} \quad (11)$$

2.5 | MFI

The MFI method can reveal relative current strength and direction quickly and without physical contact, making it suitable for use in both

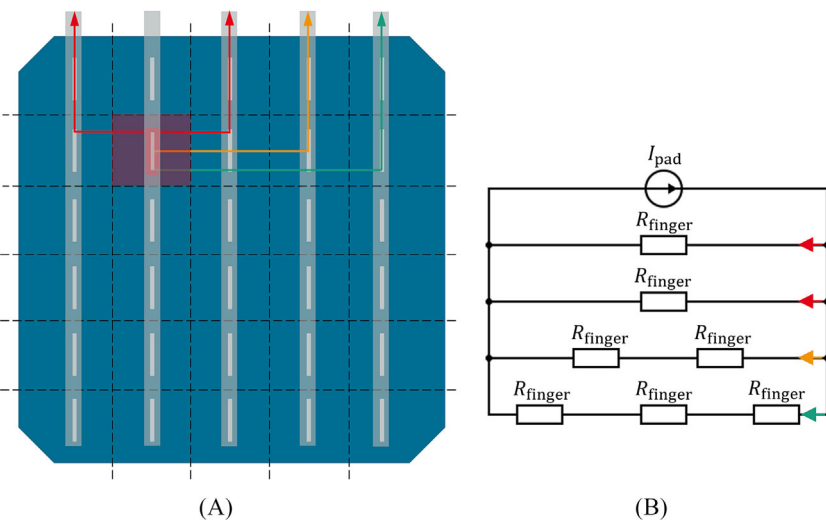


FIGURE 8 (A) Solar cell with a contact defect (highlighted in red). Dashed black lines illustrate the AOI of each contact pad. Arrows indicate the current distribution form the degraded contact pad in the neighboring busbars. (B) The current divider electrical circuit describes the distribution of the degraded pad current. Currents are color-coded.

production and field environments. Under operating conditions, PV cells or modules have a distinctive pattern of electrical current flow, which generates a magnetic field.¹² The relation between the generated magnetic flux density and the flowing electrical current is based on the Biot-Savart Law and described in Lausch et al.¹⁴

With knowledge of the current distribution, the current can be estimated from the magnetic field's measurement. Changes in the current distribution due to electrical defects alter the magnetic field's pattern, which can then be traced back to the flowing electrical currents and the defects themselves by analyzing the magnetic field distribution in all three dimensions (x, y, and z) across the solar cell or the PV module. The measurement process is as follows: the magnetic fields generated by flowing currents, either from light or electrical induction by applying voltage to the cell, can be measured by passing the magnetic field sensor over the solar cell or PV module. The closer the measurement sensor to the device, the stronger the measured signal. By analyzing the data, one can quantitatively assess the current flowing through connectors, cracks, shunts, variations in solder flux, and even individual solder points.^{12–14,19} In this work, MFI measurements are used to quantify the electrical current flowing in the ribbons and string connector by applying different string connection configurations and different contact defects scenarios.

The MFI setup used in this study (see Figure 9) consist of a magnetic field sensor array mounted to a 3-dimensional axis system from DENKweit²⁰ and an LED panel used as a light source from Bioledex.²¹ To compensate any magnetic fields from the environment, a baseline measurement is performed and subtracted from the actual measurements.

Figure 10 shows exemplary measured magnetic field generated from a current flowing in a 5-busbar cell including the resistance of the current path of each busbar. The peaks of the measured magnetic field correspond to the flowing current at each busbar of the cell. The trend of the peaks corresponds the resistance of the current path and the caused voltage drop explained in Section 2.3.

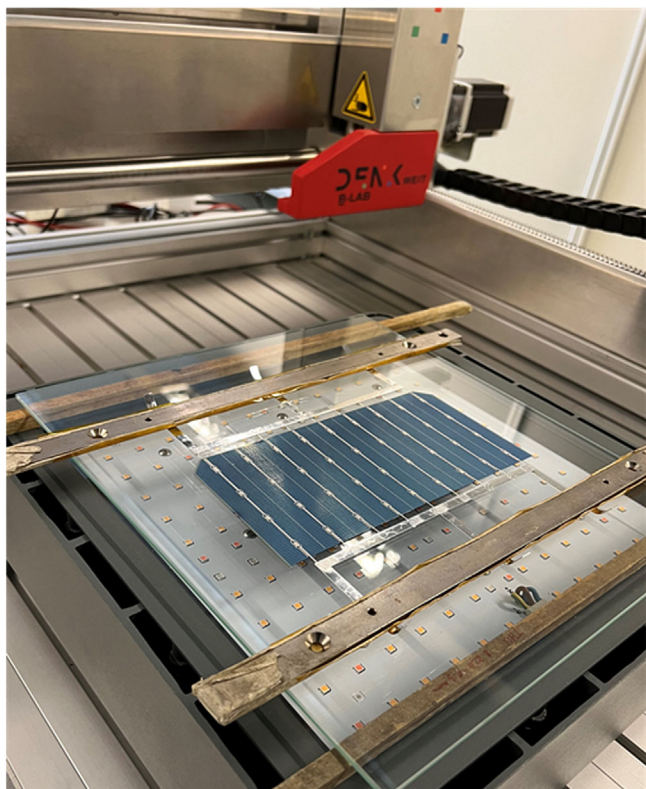


FIGURE 9 Measuring a short-circuited 9-busbar M6 half-cell by MFI using an LED panel for current generation. The red sensor array scans the sample through the 3-dimensional axis system. The cell is oriented sunny-side-down on top of the LED panel.

3 | RESULTS AND DISCUSSION

The used geometrical parameters illustrated and described in Figure 1 and Table 1 are listed in Table 2 for the simulated solar cell.

The I-V curve of the solar cell is fitted using the single-diode-model. For the fitting, the electrical parameters of the solar cell at STC

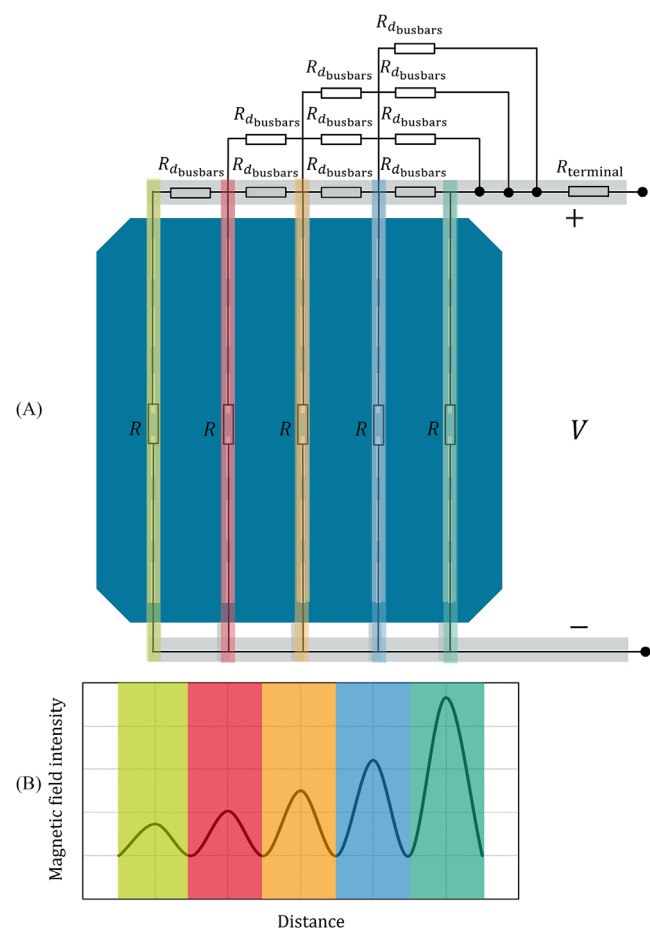


FIGURE 10 (A) Resistance of each current path of exemplary 5-busbar solar cell connected using right string connector configuration and (B) an exemplary corresponding color-coded magnetic field intensity representing the electrical current flowing in solar cell.

TABLE 2 Geometrical parameters assumed for solar cell simulation.

Symbol	Value
l_{cell}	83 mm
w_{cell}	166 mm
N_{busbar}	9
N_{pad}	6 + 1 mm pseudo-busbar (front) 4 + 1.5 mm pseudo-busbar (back)
d_{psq}	223 mm
l_{pad}	1.2 (front), 8.4 (back) mm
w_{pad}	1.4 (front), 1.6 (back) mm
d_{pads}	13 (front), 26 (back) mm
d_{busbars}	18 mm
d_{left}	11 mm
d_{right}	11 mm
d_{top}	8.23 (front), 16 (back) mm
d_{bottom}	8.23 (front), 16 (back) mm

are required. These are shown in Table 3. The geometrical and electrical parameters of the cell metallization, ribbons, and solder are based on typical values and measurements, which are reported in literature. For the sake of conciseness and to focus on the main findings of this study, the specific values and measurements are not provided here but can be made available upon request.

Using the listed simulation parameters, the current share at busbar of the 9-busbar M6 half-cell is calculated for different string connection configuration based on the approach explained in Section 2.3. Current share at busbar includes the current flowing in busbar and soldered ribbon. The simulation is done by applying a $5 \times 0.3 \text{ mm}^2$ string connector. Results are shown in Figure 11.

The results show differences in current share at busbars depending on the string connection configuration. The highest current flows in the closest busbar to the string connector terminal. However, the trend exhibits a maximum current share difference of only about 2% when applying right or left string

TABLE 3 Electrical simulation parameters of solar cell.

Symbol	Description	Value
I_{sc}	Short circuit current	5.53 A
I_{mpp}	Current at maximum power point	5.24 A
V_{oc}	Open circuit voltage	0.68 V
V_{mpp}	Voltage at maximum power point	0.57 V
P_{mpp}	Power at maximum power point	2.99 W
η	Efficiency	22.91%

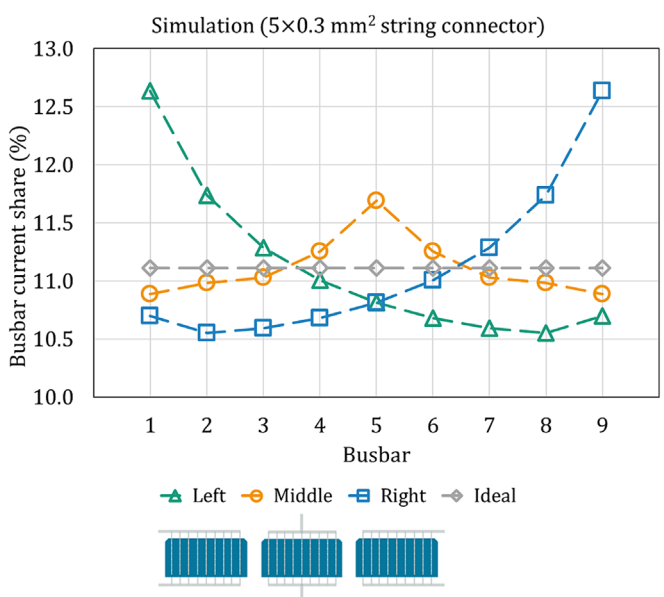


FIGURE 11 Simulated current share of a 9-busbar M6 half-cell using a $5 \times 0.3 \text{ mm}^2$ string connector with different string connection configurations. Ideal case serves as a reference. The different configurations are represented by different symbols (see legend). The dashed lines are meant as a guide to the eye.

connection configuration. This small current share difference is due to the low resistance of the string connector as it is a well-suited design for high currents. To validate the simulation results, single cell modules are built with different string connection configurations as illustrated in Figure 12A. The cell is characterized by MFI as described in Figure 9, whereby it is illuminated and short-circuited. The corresponding heatmaps of the measured magnetic flux density are shown in Figure 12B. The line scan measurement of the magnetic flux density averaged in the horizontal direction is shown in Figure 12C. MFI results in this work represent the magnitude (length of the vector) of the magnetic flux density B in x and y directions. This quantity reflects the current density within the sample plane. To indicate the direction of the current flow, the magnetic flux density must be extracted in each direction separately.

The MFI measurements do not show the trend in current share that is expected based on the results in Figure 11. This is because the inhomogeneity in current share is too low compared to other measurement inaccuracies such as non-identical contact resistances as

well as variable distance to the measuring sensor. To gain more clear results, the same solar cell is simulated and measured using a $1 \times 0.08 \text{ mm}^2$ string connector to see more inhomogeneity in current share due to higher string connector resistance and therefore higher voltage drops over it.

Applying the new string connector dimensions results in about 18 times higher resistance. As shown in Figure 13, the current share features the same trends as in Figure 11. However, due to the higher string connector resistance, a maximum difference in current share of about 18% can be noticed, compared to only about 2% using the string connector with larger cross section.

As shown in Figure 14, pronounced differences between current share at the busbars can be noticed in the MFI measurement when using the small string connector. By extracting the magnetic flux density at each busbar and calculate its share referring to the total magnetic flux at all busbars, the current share is obtained (electrical current and magnetic flux density are directly proportional to each other). The evaluated current share using the small string connector is shown in Figure 15.

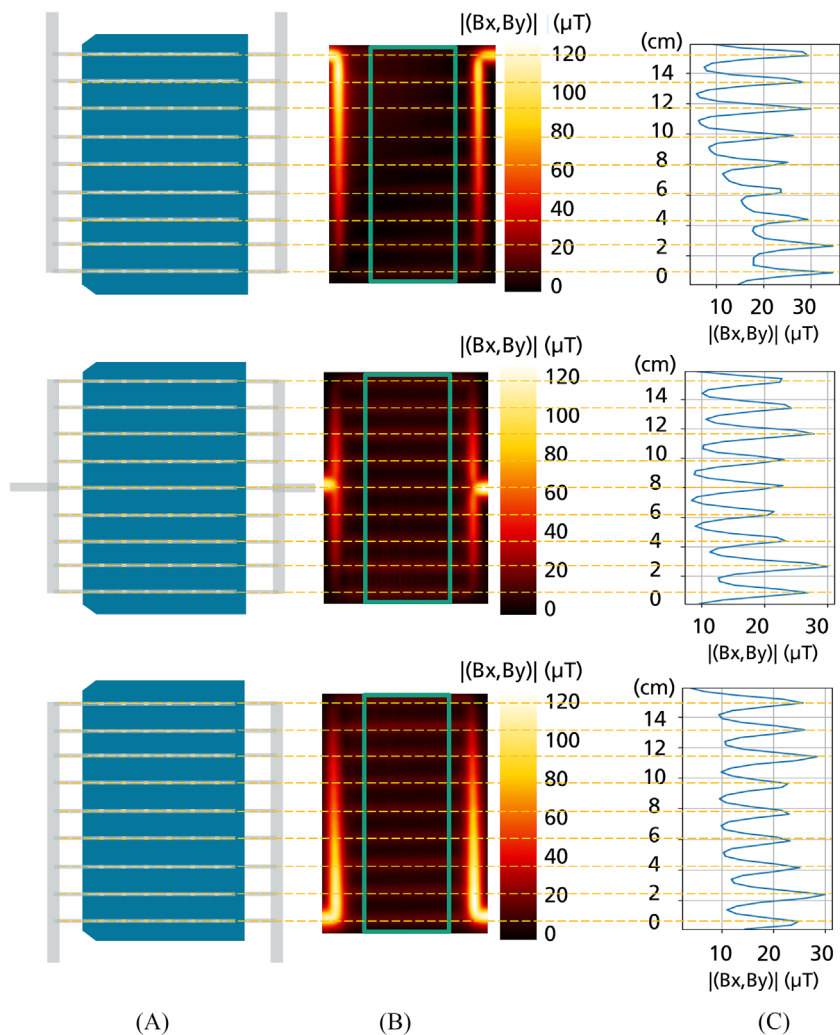


FIGURE 12 (A) Different string connection configurations applied on a 9-busbar M6 half-cell using a $5 \times 0.3 \text{ mm}^2$ string connector, (B) the corresponding MFI heatmap including the area of interest (green border), and (C) the line scan measurement of the magnetic flux density averaged in the horizontal direction within the area of interest. Orange dashed lines are meant as a guide to the eye.

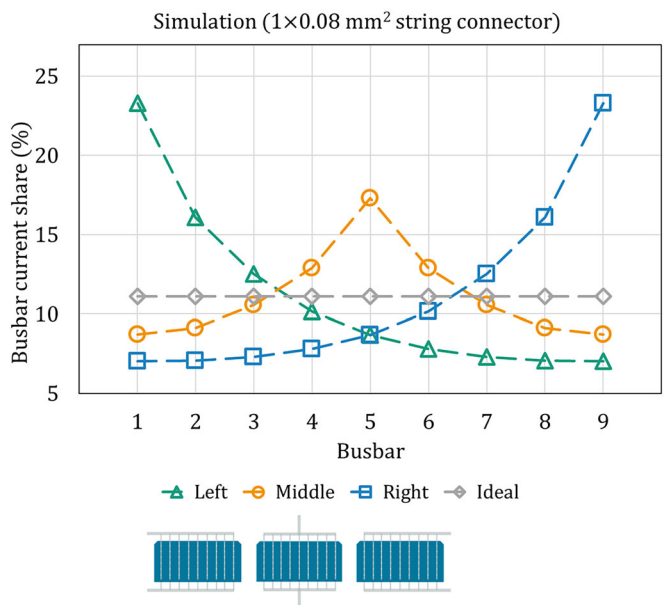
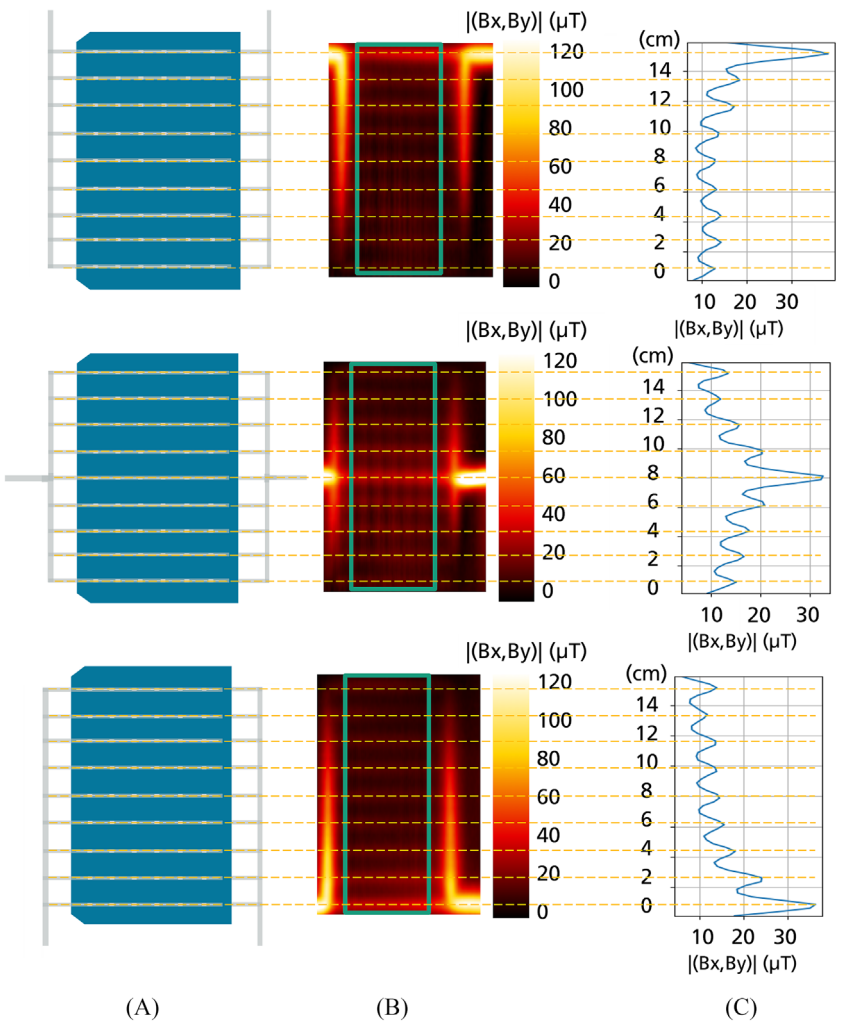


FIGURE 13 Simulated current share of a 9-busbar M6 half-cell using a $1 \times 0.08 \text{ mm}^2$ string connector with different string connection configurations. Ideal case serves as a reference. The different configurations are represented by different symbols (see legend). The dashed lines are meant as a guide to the eye.

FIGURE 14 (A) Different string connection configurations applied on a 9-busbar M6 half-cell using a $1 \times 0.08 \text{ mm}^2$ string connector, (B) the corresponding MFI heatmap including the area of interest (green border), and (C) the line scan measurement of the magnetic flux density averaged in the horizontal direction within the area of interest. Orange dashed lines are meant as a guide to the eye.



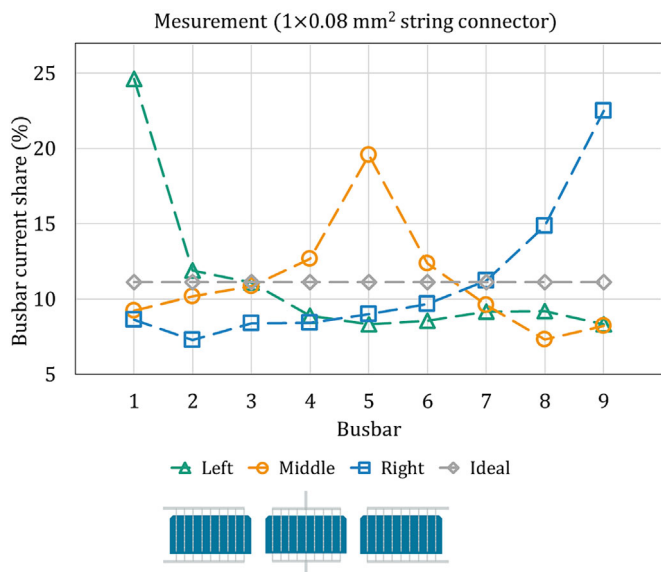


FIGURE 15 Calculated current share of a 9-busbar M6 half-cell using a $1 \times 0.08 \text{ mm}^2$ string connector with different connection configurations, derived from the MFI measurements shown in Figure 14. Ideal case serves as a reference. The different configurations are represented by different symbols (see legend). The dashed lines are meant as a guide to the eye.

In Figure 15, the same trend of current share as in simulation results can be noticed. From the MFI measurements, a maximum difference in current share of about 17.3% is obtained, which is in a good agreement with the 18% maximum difference in the simulation results shown in Figure 13. Using the middle configuration results in about 20% of the cell current passing at the middle busbar compared to about 11% in the ideal case. In left or right connection configurations, which are used in strings within modules, 25% of the cell current flows at the busbar near the string connector terminal compared to about 11% in the ideal case.

Since the ohmic electrical loss is the product of the electrical resistance and the square of the magnitude of the flowing current, the inhomogeneous current distribution results in higher power losses compared to the ideal case. The increase in ohmic losses is not only due to the flow of inhomogeneous current in ribbons but also because of the collected ribbon currents in string connector. The amount of current in each string connector section depends on the position of the string connector terminal.

In Figure 16, the ohmic losses in ribbons and string connector as well as the power at maximum power point of solar cell are shown for different string connection configurations. The current flow in the string connector contributes to about 85% of the ohmic losses, while the remaining 15% are due to current flow in the ribbons. Connecting the string connector terminal to the leftmost or rightmost ribbon results in about 1.1 W ohmic losses compared to about 0.7 W when connecting the string connector terminal to the ribbon at the middle. To validate that, the I-V curve of the solar cell is measured by applying the three different connection configurations. The maximum power

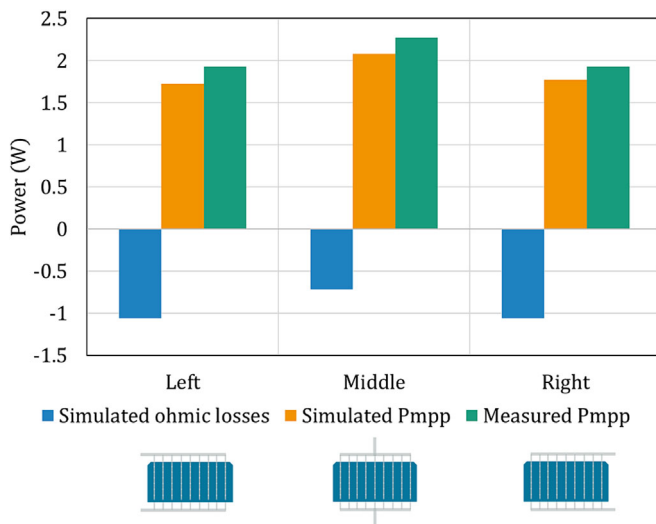


FIGURE 16 Simulated ohmic losses (blue), simulated power at maximum power point (orange), and measured power at maximum power point (green) of a 9-busbar M6 half-cell power using a $1 \times 0.08 \text{ mm}^2$ string connector with different connection configurations (see legend).

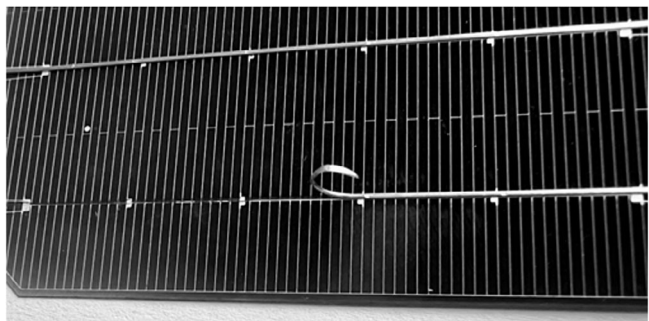


FIGURE 17 Partial detachment of a ribbon for measurement purposes.

point of the cell with its terminal at the middle busbar is higher than the other two configurations by about 0.35 W, which is in a good agreement with simulation results.

On module level, strings are interconnected to each other in series or parallel using either left or right string connection configuration. Assuming that only cells that are directly connected to the string connector are affected, only two cells per string contribute to additional ohmic loss due to current inhomogeneity on cell level. Using the current share results, the increase of power loss in the ribbons due to right or left connection configuration compared to ideal case can be calculated. The power loss in ribbons increases by about 22% for the solar cell sides that are directly connected to the string connector, that is, front side of top cell and rear side of bottom cell of each string in the module. Furthermore, current inhomogeneity causes

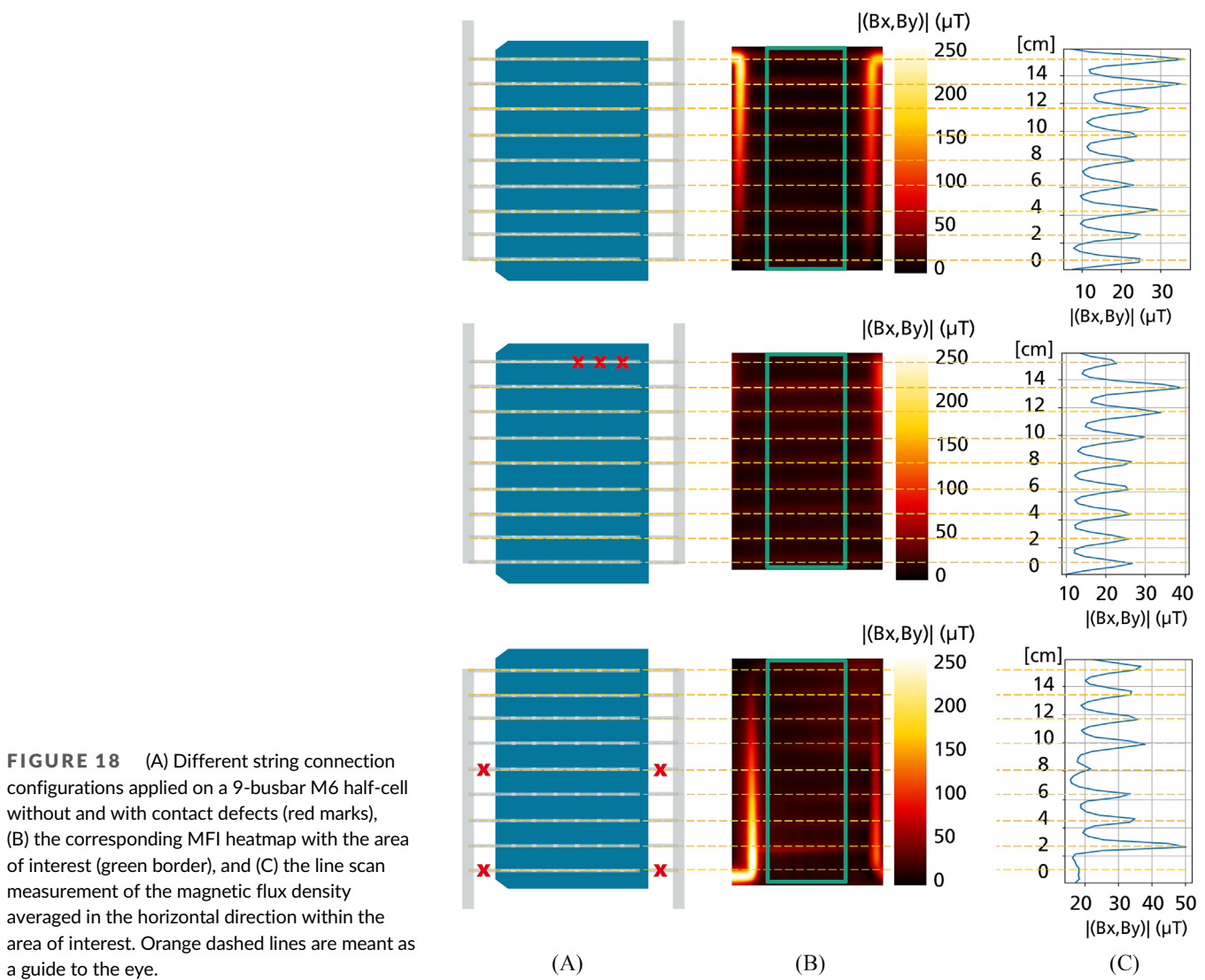
an increase of about 30% in ohmic losses in string connector compared to the case of ideally distributed ribbon currents. Considering a 120-half-cell module containing 12 strings, the affected 24 cells with the current inhomogeneity will increase the ohmic loss of the module by about 7.7 W, which is about 2.1% of a 359 Wp module using the solar cell with the electrical parameters shown in Table 3. The calculated module power loss assumes applying the $1 \times 0.08 \text{ mm}^2$ string connector to the module. Normally, a string connector with larger cross section is used, resulting in a reduced negative impact of the current inhomogeneity on the module power. Nonetheless, specific module designs may necessitate the use of thin string connectors to minimize module area or avoid internal shading, particularly when placing the string connector on the cell's active area is unavoidable.

Regarding contact defects between metallization and ribbons, the 9-busbar M6 half-cell is simulated considering complete contact failure between the ribbon and half of the pads of the 1st busbar. For the validation measurement, the ribbon is detached as shown in Figure 17.

The cell with the detached ribbon is measured by applying MFI as shown in Figure 18. The cell is connected using a $5 \times 0.3 \text{ mm}^2$ string connector. Before detaching the ribbon, the cell exhibits mostly homogenous magnetic flux densities at all busbars. However, the current at the first and second busbars seem to be higher than at the other busbars.

The increase in carried current at the top two busbars compared to others can be explained with different factors such as solder connection quality and therefore different contact resistance between each ribbon and the string connector. Non-flat placement of the solar cell as well as bended connectors can affect the distance between the sensor and the current path, which impacts the measured magnetic flux density as well. Furthermore, inaccuracies in the measuring system can be responsible for additional deviation, such as inhomogeneity of the used LED panel. Figure 19 exemplary shows a case, where the solar cell is not perfectly flat on the LED panel and the ribbons are slightly arched upwards.

Detaching the ribbon from three of the six pads of the busbars results in a decrease in the current at that ribbon and an



increase in the current at the other ribbons, especially the neighboring ones.

Figure 20 shows the simulated and measured current distribution for the cell with detached ribbon as shown in Figure 18 (middle). Except for the evaluated current of first two busbars out of the measured magnetic field, the trend of simulated current share at all busbars after applying the contact failure is in a good agreement with measurement. A maximum deviation in current share of about 2.5% can be explained with the previously mentioned reasons. While repeating measurement, ribbons are partially and fully detached due to connector flexing while contacting (see Figure 21). The redistribution of currents in Figure 18 can be assessed compared to the case, where no contact failure is applied.

To investigate the impact of contact failure on the cell power and efficiency in more details, various contact failure at certain contact pads, ribbons, and string connectors are simulated.

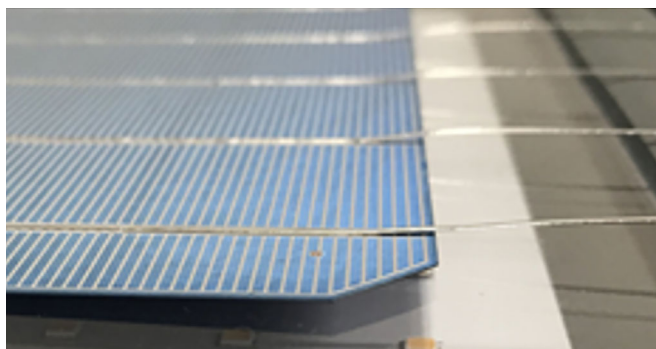


FIGURE 19 Non-flat placement of solar cell and on the LED panel and slightly lifted ribbons while performing MFI measurement.

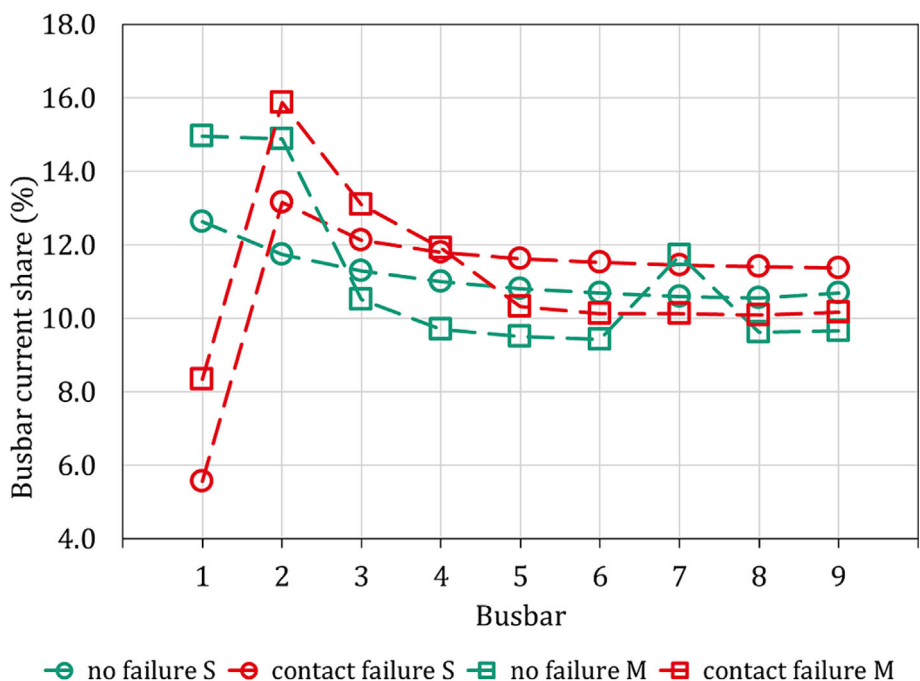


FIGURE 20 Comparison between simulation (circles) and measurement (squares) regarding the current distribution without (green) and with (red) contact failure at three pads at a busbar in a 9-busbar M6 half-cell. Dashed lines are meant as a guide to the eye.

Figure 22 shows the change in power of the solar cell at maximum power point and in efficiency applying different types of contact defects. Figure 22A shows that contact failure at contact pads has more impact on cell power and efficiency, when the contact failure is in busbar that is closer to the string connector terminal. Completely detaching one ribbon has same consequences as shown in Figure 22B, where detaching the nearest ribbon to the terminal causes the highest power and efficiency loss. Cumulatively detaching ribbons as shown in scenarios 19–25 results in clearly higher additional ohmic losses and power losses. For example, detaching one ribbon would result in about 0.2%_{abs} less cell efficiency, whereas detaching five ribbons results in about 2.1%_{abs} less efficiency. Figure 22C shows that the impact of string connector breakage is

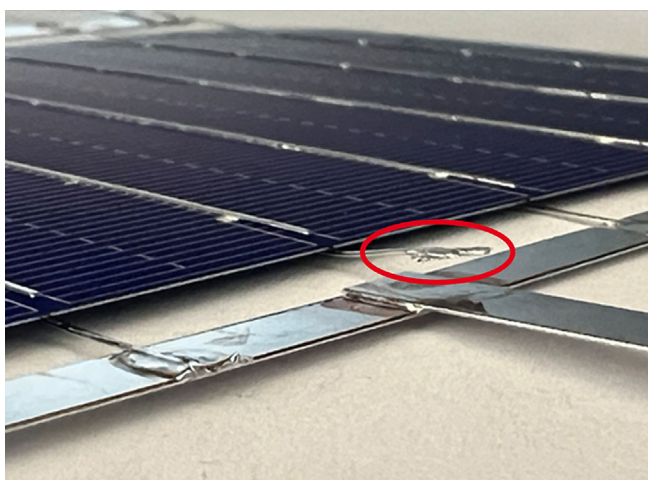
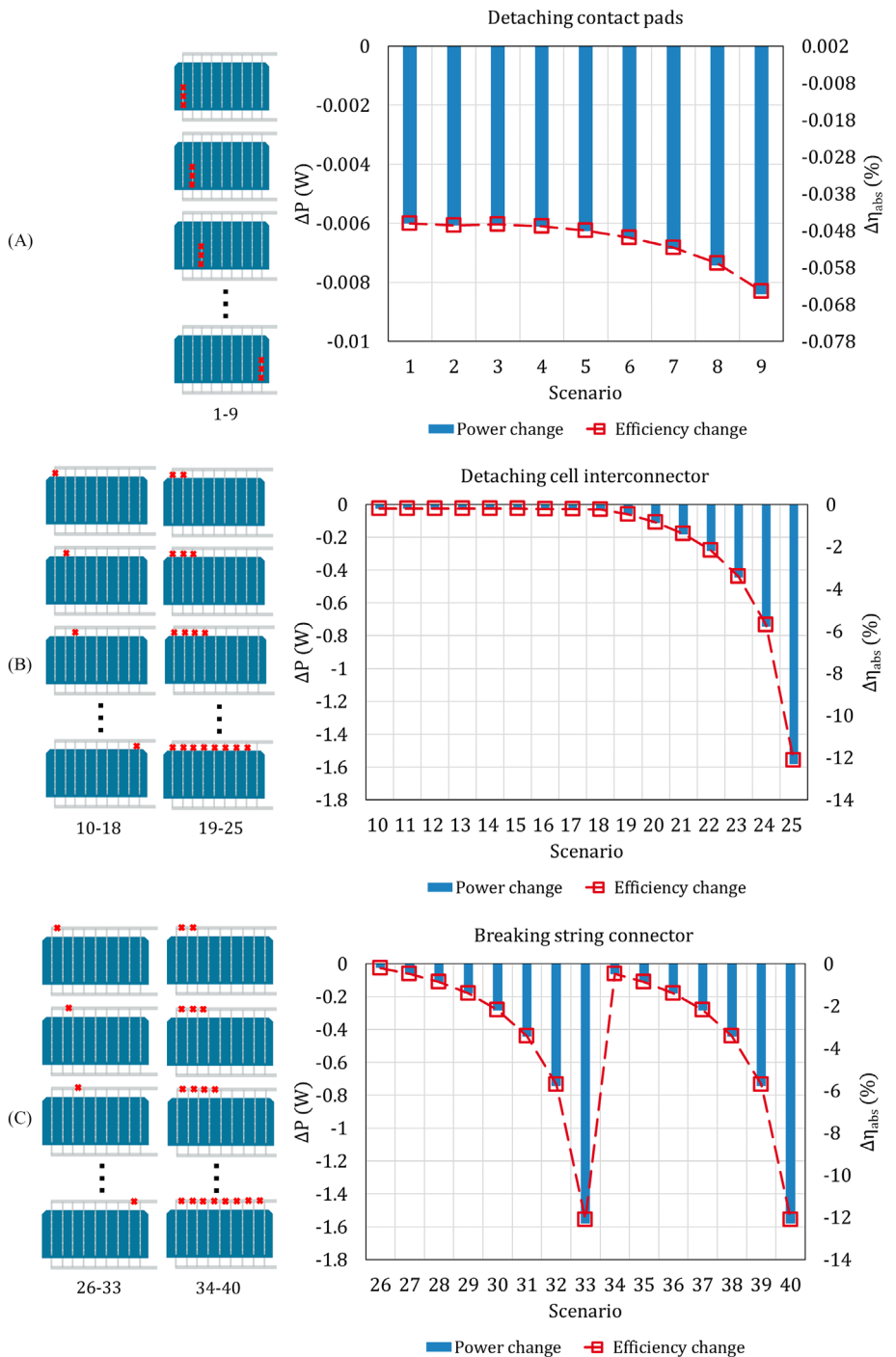


FIGURE 21 Detached center ribbon from the string connector.

FIGURE 22 Simulated change in cell power at maximum power point (blue columns) and efficiency (red squares) applying different contact failure scenarios by (A) detaching contact pads, (B) completely detaching ribbons, and (C) breaking string connector. The contact failure scenarios are numbered consecutively and shown on the left side of each diagram. Red marks on solar cells represent the contact failure. Dashed lines are meant as a guide to the eye.



higher compared to detaching contact pads and ribbons. Breaking the string connector at the point just before the ribbon that is connected to the string connector terminal (scenario 33) leads to a reduction in cell power of about 1.58 W. Cumulatively breaking several string connectors (scenarios 34–40) does not have higher impact on the cell power and efficiency, since the point, where breakage takes place, already eliminates all previous ribbons. Therefore, not the amount of broken string connector points is the crucial parameter, but the position of it.

When examining a 120-half-cell module with one outer misaligned ribbon in all cells of each string possibly caused during the soldering process by the stringer machine (see Figure 23), it's estimated to incur a reduction of approximately 3 W in module power output. This decrease translates to approximately 0.8% of the module's total power (359 W). This assessment assumes that the misaligned ribbon fails to establish any contact to the cells in the string, thereby rendering them non-contributory to the overall current flow within the module. However, in a laminated module, the

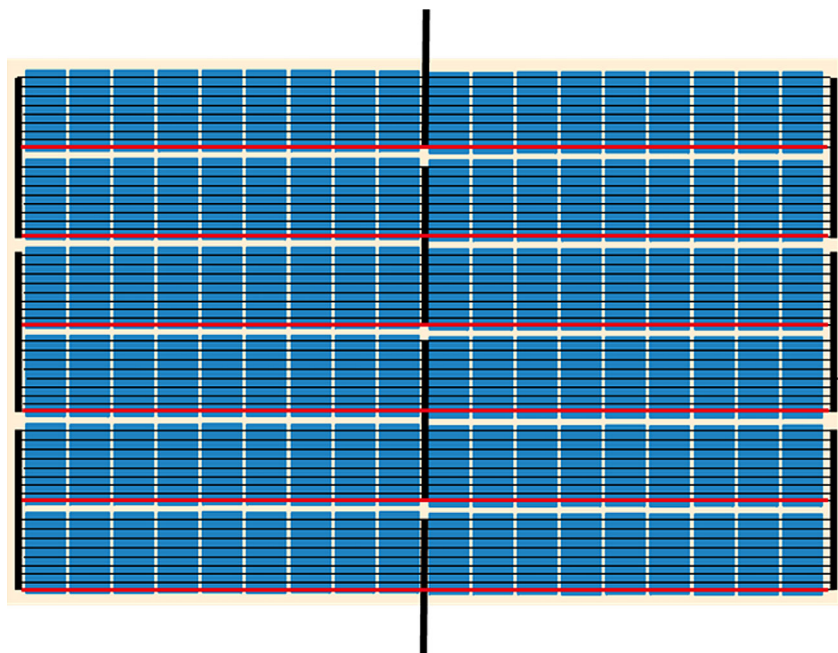


FIGURE 23 120-half-cells module with misaligned outer ribbon along its strings (red marked).

misaligned ribbon would not be completely disconnected from the cells, as the laminated module would compel contact between the ribbon and cells. This contact leads to a partial contribution to current flow, thereby reducing the power loss due to the misalignment. Therefore, this assessment may overestimate the actual impact.

4 | SUMMARY AND OUTLOOK

This work shows the impact of the position of string connector terminal as well as its dimensions on the current share at the busbars of a solar cell and therefore on the cell power and efficiency. Furthermore, this study presents the influence of different contact defects scenarios on the solar cell power and efficiency. Simulation and measurement results show that due to the string connection and the position of its terminal, the currents flowing in each ribbon in a solar cell cannot be evenly distributed. This is because each busbar has its own current path with ohmic resistance that differs from other busbars. Results show that the nearest busbar to the string connector terminal carries the highest current due to lower ohmic resistance of the current path. Left or right string connection configurations cause more inhomogeneity and therefore more additional ohmic losses compared to middle string connection configuration. Applying smaller string connector results in higher ohmic resistance, which leads to more current inhomogeneity and additional ohmic losses. Applying $1 \times 0.08 \text{ mm}^2$ string connector with center connection configuration results in about 0.35 W less ohmic loss compared to left and right connection configurations. On module level, considering a 120-half-cell module using the chosen M10 half-cell and the small string connector in this study, results show a reduction of about 2.1% of total module power

compared to the ideal case, where cell current is evenly distributed over busbars. Regarding contact failure, results show that the position of busbar, where contact failure takes place, does affect the additional ohmic losses. The highest additional ohmic losses result from contact failure at busbar that is closer to the string connector terminal. Simulation results show that detaching one ribbon would cause about 0.2%_{abs} decrement in cell efficiency. Detaching two ribbons at the same time would result in about 0.47%_{abs} less cell efficiency. On module level, results show that a completely misaligned ribbon along all strings in the module could lead to a power loss of about 0.8%.

This study enlightens the impact of string connection on solar cell and module level, especially when resizing it by reducing its width and thickness. The reason for such a cross section reduction could be a module design requirement to increase module efficiency to eliminate inactive module areas, where string connectors are placed. Furthermore, some designs of bifacial modules require the presence of string connectors behind the backside of the solar cells, which causes internal shading and therefore power losses. In that case, using thinner string connectors would reduce the negative impact of the internal shading. However, the impact of thin string connectors on the current distribution and therefore on ohmic losses and cell power and efficiency must be taken to account. By utilizing the developed model, it is possible to optimize the dimensions of the string connectors to achieve both low series resistance and minimal material consumption.

ACKNOWLEDGEMENTS

The authors acknowledge the funding of the work by the German Ministry of Economic Affairs and Energy under grant no. 03EE1028A “CTS1000plus”. Open Access funding enabled and organized by Projekt DEAL.

DATA AVAILABILITY STATEMENT

The data that support the findings of this study are available from the corresponding author upon reasonable request.

ORCID

Ammar Tummalieh  <https://orcid.org/0000-0001-8891-8235>

Julian Weber  <https://orcid.org/0000-0001-5679-2586>

REFERENCES

1. Guo S, Ma F-J, Hoex B, Aberle A, Peters M. Analysing solar cells by circuit modelling. *Energy Procedia*. 2012;25:28-33. doi:[10.1016/j,egypro.2012.07.004](https://doi.org/10.1016/j,egypro.2012.07.004)
2. Haedrich I, Eitner U, Wiese M, Wirth H. Unified methodology for determining CTM ratios: systematic prediction of module power. *Solar Energy Mater Solar Cells*. 2014;131:14-23. doi:[10.1016/j.solmat.2014.06.025](https://doi.org/10.1016/j.solmat.2014.06.025)
3. Mittag M, Zech T, Wiese M, Bläsi D, Ebert M, Wirth H. "Cell-to-module (CTM) analysis for photovoltaic modules with shingled solar cells: 44th IEEE photovoltaic specialists conference," 2017.
4. Mittag M, Pfreundt A, Shahid J, Wöhrle N, Neuhaus DH. "Techno-economic analysis of half cell modules—the impact of half cells on module power and costs," 2019.
5. Yousuf H, Zahid MA, Khokhar MQ, et al. Cell-to-module simulation analysis for optimizing the efficiency and power of the photovoltaic module. *Energies*. 2022;15(3):1176. doi:[10.3390/en15031176](https://doi.org/10.3390/en15031176)
6. Höffler H, Haunschmid J, Rein S. Influence of external contacting on electroluminescence and fill factor measurements. *Solar Energy Mater Solar Cells*. 2016;152:180-186. doi:[10.1016/j.solmat.2016.03.039](https://doi.org/10.1016/j.solmat.2016.03.039)
7. Zekry A, Al-Mazroo AY. A distributed SPICE-model of a solar cell. *IEEE Trans Electron Devices*. 1996;43(5):691-700. doi:[10.1109/16.491244](https://doi.org/10.1109/16.491244)
8. Rajput AS, Rodríguez-Gallegos CD, Ho JW, et al. Fast extraction of front ribbon resistance of silicon photovoltaic modules using electroluminescence imaging. *Solar Energy*. 2019;194:688-695. doi:[10.1016/j.solener.2019.11.013](https://doi.org/10.1016/j.solener.2019.11.013)
9. Rendler LC, Kraft A, Ebert C, Wiese S, Eitner U. "Investigation of thermomechanical stress in solar cells with multi busbar interconnection by finite element modeling," in *Proceedings of the 32nd European Photovoltaic Solar Energy Conference and Exhibition*, Munich, Germany, 2016, pp. 94-98.
10. Kumar S, Meena R, Gupta R. Finger and interconnect degradations in crystalline silicon photovoltaic modules: a review. *Solar Energy Mater Solar Cells*. 2021;230:111296. doi:[10.1016/j.solmat.2021.111296](https://doi.org/10.1016/j.solmat.2021.111296)
11. Dost G, Höffler H, Greulich JM. Advanced series resistance imaging for silicon solar cells via electroluminescence. *Phys Status Sol (A)*. 2021;218(6):2000546. doi:[10.1002/pssa.202000546](https://doi.org/10.1002/pssa.202000546)
12. Weber J, Hoffmann S, Kaufmann K, De Rose A. Magnetic field imaging (MFI) of shingle solar modules. In: *2022 IEEE 49th Photovoltaics Specialists Conference (PVSC), Philadelphia, PA, USA*; 2022:231. doi:[10.1109/PVSC48317.2022.9938644](https://doi.org/10.1109/PVSC48317.2022.9938644)
13. Zeller U, Lausch D, Pander M, Kaufmann K, Slaby S, Schoenfelder S. "Comparison of magnetic field imaging (MFI) and magnetic field simulation of silicon solar cells," *SiliconPV*, 2019.
14. Lausch D, Patzold M, Rudolph M, Lin C-M, Fröbel J, Kaufmann K. "Magnetic field imaging (MFI) of solar modules," *Proceedings of the 35th European Photovoltaic Solar Energy Conference and Exhibition EUPVSEC*, 2018, doi:[10.4229/35thEUPVSEC20182018-5BO.11.5](https://doi.org/10.4229/35thEUPVSEC20182018-5BO.11.5)
15. Chan D, Phang J. Analytical methods for the extraction of solar-cell single- and double-diode model parameters from I-V characteristics. *IEEE Trans Electron Devices*. 1987;34(2):286-293. doi:[10.1109/T-ED.1987.22920](https://doi.org/10.1109/T-ED.1987.22920)
16. Islam MN, Rahman MZ, Mominuzzaman SM, "The effect of irradiation on different parameters of monocrystalline photovoltaic solar cell," pp. 1-6, doi:[10.1109/ICDRET.2014.6861716](https://doi.org/10.1109/ICDRET.2014.6861716)
17. Tummalieh A, Paritala B, Mittag M, Neuhaus DH. "Interconnection technology in PV modules: impact of ribbons, tab connectors and electrically conductive backsheet on module performance," in *Proceedings of the 8th World Conference on Photovoltaic Energy Conversion*, Milan, Italy, 2022.
18. Reichman J. The current-voltage characteristics of semiconductor-electrolyte junction photovoltaic cells. *Appl Phys Lett*. 1980;36(7):574-577. doi:[10.1063/1.91551](https://doi.org/10.1063/1.91551)
19. DENKweit. B-TECH A new access to direction and strength of electric currents. [Online]. Available: https://denkweit.com/wp-content/uploads/2020/08/DENKweit_B-TECH_solar_en_short.pdf (accessed: Jun. 4 2023).
20. DENKweit. [Online]. Available: <https://denkweit.com/en/> (accessed: Jun. 5 2023).
21. Bioledex. [Online]. Available: <https://www.bioledex.de/> (accessed: Jun. 5 2023).

How to cite this article: Tummalieh A, Mittag M, Weber J, et al. Impact of string connection and contact defects on electrical current distribution in solar cells and modules: A model validated by magnetic field imaging. *Prog Photovolt Res Appl*. 2025;33(1):219-235. doi:[10.1002/pip.3806](https://doi.org/10.1002/pip.3806)